

Highest Fusion Performance without Harmful Edge Energy Bursts in Tokamak

S.K.Kim*,¹ R.Shousha*,² S.M.Yang*,¹ Q.Hu,¹ S.H.Hahn,³ A.Jalalvand,² J.-K.Park,⁴ N.C.Logan,⁵ A.O.Nelson,⁵ Y.-S.Na,⁴ R.Nazikian,⁶ R.Wilcox,⁷ R.Hong,⁸ T.Rhodes,⁸ C.Paz-Soldan,⁵ Y.M.Jeon,³ M.W.Kim,³ W.H.Ko,³ J.H.Lee,³ A.Bathey,⁵ G.Yu,⁹ A.Bortolon,¹ J.Snipes,¹ and E.Kolemen^{1,2, a)}

¹⁾*Princeton Plasma Physics Laboratory*

²⁾*Princeton University*

³⁾*Korea Institute of Fusion Energy*

⁴⁾*Seoul National University*

⁵⁾*Columbia University*

⁶⁾*General Atomics*

⁷⁾*Oak Ridge National Laboratory*

⁸⁾*University of California Los Angeles*

⁹⁾*University of California Davis*

(Dated: May 10, 2024)

The path of tokamak fusion and ITER is maintaining high-performance plasma to produce sufficient fusion power. This effort is hindered by the transient energy burst arising from the instabilities at the boundary of high-confinement plasmas. The application of 3D magnetic perturbations is the method in ITER and possibly in future fusion power plants to suppress this instability and avoid energy busts damaging the device. Unfortunately, the conventional use of the 3D field in tokamaks typically leads to degraded fusion performance and an increased risk of other plasma instabilities, two severe issues for reactor implementation. In this work, we present an innovative 3D field optimization, exploiting machine learning, real-time adaptability, and multi-device capabilities to overcome these limitations. This integrated scheme is successfully deployed on DIII-D and KSTAR tokamaks, consistently achieving reactor-relevant core confinement and the highest fusion performance without triggering damaging instabilities or bursts while demonstrating ITER-relevant automated 3D optimization for the first time. This is enabled both by advances in the physics understanding of self-organized transport in the plasma edge and by advances in machine-learning technology, which is used to optimize the 3D field spectrum for automated management of a volatile and complex system. These findings establish real-time adaptive 3D field optimization as a crucial tool for ITER and future reactors to maximize fusion performance while simultaneously minimizing damage to machine components.

*These authors equally contributed to this work.

For a fusion energy source to be economically competitive in the global energy market, it must produce a high fusion triple product ($n\tau T$)¹ with sufficient plasma density (n), temperature (T), and energy confinement time (τ) while sustaining fusion reactions. In other words, the fusion plasma requires sufficient figure of merit ($G \propto n\tau T$)^{1,2}, which increases with plasma confinement quality (H_{89})³, where H_{89} is normalized energy confinement time. For example, the International Thermonuclear Experimental Reactor (ITER) requires $G_{\text{fus}} > 0.4$ and $H_{89} > 2$ to achieve¹ its objective (A fusion power ten times higher than the input heating power). One of the leading approaches⁴ towards this goal is a tokamak operated robustly in the high confinement mode (H-mode)⁵, characterized by a narrow edge transport barrier (or confinement pedestal) responsible for significantly elevated plasma pressures within the device. This "pedestal" has demonstrated notable benefits by enhancing G , thereby improving the fusion economy. However, the H-mode has a high-pressure gradient at the edge (pedestal), which introduces significant risks to reactor operation, mainly due to emerging dangerous edge energy bursts as a result of a plasma instability known as edge localized modes (ELMs)⁶. These edge bursts cause rapid relaxations in pedestal plasma energy, leading to intense transient heat fluxes on reactor walls, resulting in undesirable material erosion and surface melting. The predicted heat energy reach $\sim 20\text{MJ}/\text{m}^2$, unacceptable in a fusion reactor^{7,8}. Consequently, for tokamak designs to become a viable option for fusion reactors, reliable methods must be developed to routinely suppress edge burst events without affecting G .

Resonant magnetic perturbations (RMPs) using external 3D field coils^{10–13} have proven to be one of the most promising methods for edge burst control. The typical external coils surrounding the plasma to generate 3D fields are shown in Fig. 1. By reducing the pedestal^{14–24}, 3D-fields effectively stabilizes energy burst in the edge region²⁵. This stabilizing effect holds significant advantage, and therefore, the ITER baseline scenario relies on 3D-field to achieve an edge-burst-free burning plasma in a tokamak for the first time.

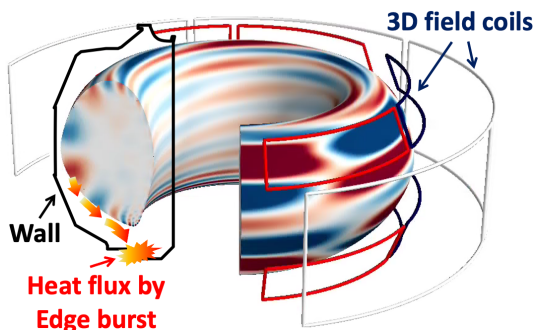


Figure 1. **3D-field coil structure in tokamak.** Schematic diagram of 3D field coil and edge energy-burst in DIII-D tokamak. Color contour shows typical 3D-field amplitude formed by coils.

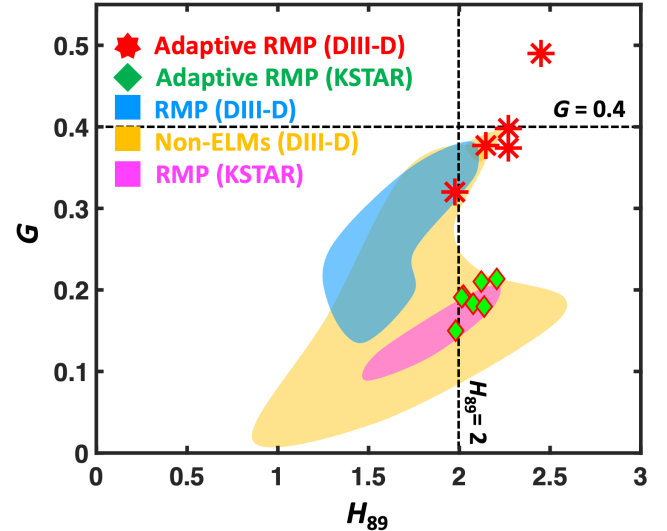


Figure 2. **Performance comparison of ELM-free discharges in DIII-D and KSTAR tokamaks.** H_{89} versus figure of merit (G) at ELM-free state. These cover various non-ELMing scenarios, including RMP, QH, L-mode, I-mode, and EDA-H mode in DIII-D. The red star and green diamond markers show the adaptive RMP discharges in DIII-D and KSTAR, respectively. The dashed lines indicate ITER-relevant level^{1,9} required to achieve their objectives. A detailed plot for this figure can be found in the supplement material.

However, this scenario comes at a significant cost, resulting in a significant deterioration of H_{89} and G compared to standard high-confinement plasma regimes, thus depleting economic prospects. Moreover, the 3D field also raises the risk of disastrous core instability, known as a disruption, which is even more severe than an edge burst. Thus, the safe accessibility and compatibility of edge-burst-free operation with high confinement operation requires urgent exploration.

This work reports on an innovative and integrated 3D-field optimization on both KSTAR and DIII-D tokamaks for the first time by combining machine learning (ML), adaptive^{26,27}, and multi-machine capabilities for automatically accessing and achieving an almost fully edge-burst-free state while boosting the plasma fusion performance from its initial burst-suppressed state, which is a significant milestone toward edge-burst-free operation for future reactors. This is accomplished by real-time exploitation of hysteresis between edge-burst-free onset and loss to enhance plasma confinement while extending the ML capability in capturing physics and optimizing nuclear fusion technology^{28–30}.

This integration facilitates 1) highly enhanced plasma confinement, reaching the highest fusion G (see Fig. 2) among ELM-free scenarios in two machines with the increase in G up to 90%, 2) fully automated 3D-field optimization for the first time by using an ML-based 3D-field simulator, and 3) concurrent establishment of burst suppression from the very beginning of the plasma operation, achieving nearly complete edge-burst-free operation close to the ITER-relevant level. Such an achievement paves a vital step for future devices such as ITER, where relying on empirical RMP optimization

^{a)}Corresponding author: ekolemen@princeton.edu

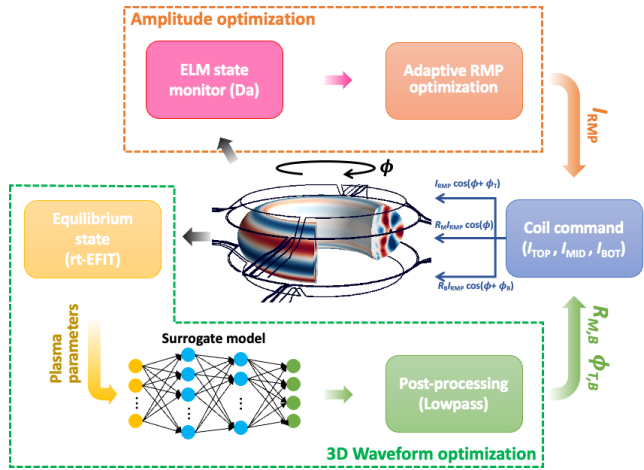


Figure 3. **Machine-learning based real-time RMP optimization algorithm.** Schematic diagram of integrated RMP optimization scheme in KSTAR with ML-surrogate model (ML-3D).

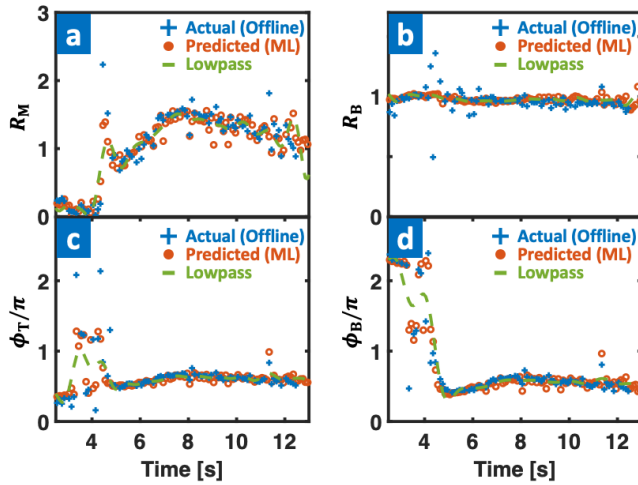


Figure 4. **ML-3D model performance.** **a-d** Validating comparison of the model using test case, showing actual (blue), predicted (orange), and low-pass filtered (green) $R_{M,B}$, $\phi_{T,B}$ values in time.

is no longer a viable or acceptable approach.

This paper is organized as follows. We first explain the integrated 3D-field optimization algorithms. The contribution of ML and adaptive schemes in the optimization process is introduced in the following sections. Then, the utilization of early 3D (or RMP) algorithms toward a complete ELM-free operation and underlying physics phenomena allowing the burst-free operation with high G are presented. Lastly, the discussions on the application in ITER and future reactors are drawn in summary.

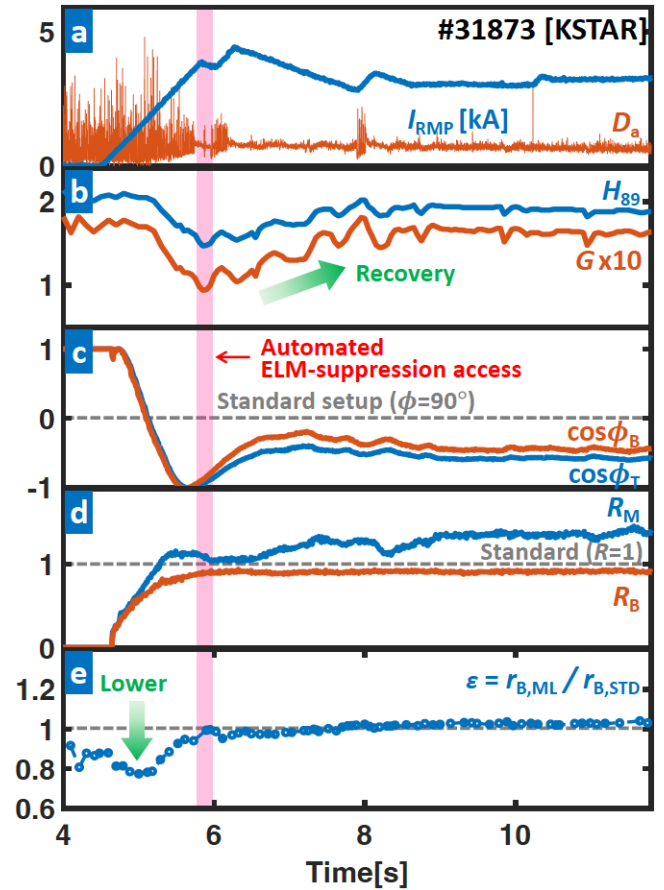


Figure 5. **Plasma parameters for a fully automated ELM suppression discharge (#31873) with integrated RMP optimization.** **a** I_{RMP} (blue) and D_α emission (orange) near outer divertor target. **b** H_{89} (blue) and G (orange). **c** Phasing between top/middle (ϕ_T , blue) and middle/bottom coils (ϕ_B , orange). **d** Current amplitude ratio between top/middle (R_M , blue) and top/bottom coils (R_B , orange). **e** Ratio ($\epsilon = r_{B,ML} / r_{B,STD}$) of 3D-coil induced r_B from ML-3D ($r_{B,ML}$) and predicted one using an empirical configuration ($r_{B,STD}$). Smaller ϵ means lower r_B than the one by standard (empirical) setup. The gray dotted line in **c,d** shows the 3D-coil configurations from a standard (empirical) setup. The red-colored area highlights the automated access to the ELM-suppressed state without pre-programmed 3D fields. The optimization algorithm is triggered at 4.5 s

I. RESULTS

Fully automated optimization of 3D-field using ML-surrogate model. The key to stable and robust ELM suppression is maintaining a sufficient edge 3D field (B_{edge}) for the ELM suppression while minimizing the core perturbation (B_{core}) or $r_B = B_{core} / B_{edge}$ to avoid disruption. B_{edge} and r_B can be controlled by adjusting the RMP current (or amplitude, I_{RMP}) and current distribution among external 3D coils (e.g. 3D waveform). For these reasons, in the present experiments, a series of discharges are used to find an optimized 3D waveform for safe ELM suppression. The successful ELM suppression in the previous studies also relies on the empirically derived 3D setup. However, this trial-and-error approach isn't

viable in a fusion reactor, where a single unmitigated disruption terminates the machine's life. Achieving reliable ELM suppression in a reactor requires a first-principle strategy to determine the 3D waveform adaptively.

In this context, this work introduces the machine learning technique to develop the novel path of automated 3D coil optimization and demonstrate the concept for the first time. This approach exploits the physics-based optimization scheme of 3D waveform³¹ based on plasma equilibrium and ideal 3D response from GPEC simulation³². This method has been validated across multiple devices^{33,34} and extensively tested on KSTAR, which has flexible 3D coils with three rows, resembling ITER's configuration. This approach effectively predicts the optimal 3D coil setup that minimizes r_B to ensure safe ELM suppression. However, its computational time, taking tens of seconds, hinders real-time applicability, limiting its use to pre-programmed or feed-forward strategies.

To overcome such limitations, a surrogate model (ML-3D) of GPEC code has been developed to leverage the physics-based model in real time. This model uses machine learning algorithms to accelerate the calculation time to the "ms" scale, and it is integrated into the adaptive RMP optimizer in KSTAR. ML-3D consists of a fully connected multi-layer perceptron (MLP) which is driven by nine inputs, the total plasma current (I_p), edge safety factor (q_{95}), global poloidal beta (β_p), global internal inductance (l_i), the coordinates of X-points on the R-Z plane (R_X, Z_X), and the plasma elongation (κ). These parameters are derived from real-time equilibrium³⁵ calculations and are normalized to have zero mean and unit variance per input feature overall training set. The outputs of the model are coil configuration parameters (R_M, R_B, ϕ_T, ϕ_B), which determines the relations between coil current distribution across the top (I_{TOP}), middle (I_{MID}), and bottom (I_{BOT}) 3D coils. Here, $R_M = I_{MID}/I_{TOP}$, $R_B = I_{BOT}/I_{TOP}$, and $\phi_{T,B}$ is the toroidal phasing of the top and bottom coil currents relative to the middle coil (see Fig. 3). In order to train this model, the GPEC simulations from 8490 KSTAR equilibria are utilized.

As shown in Fig. 3, the algorithm adaptively changes I_{RMP} in real-time by monitoring the ELM state using D_α signal. This maintains a sufficient edge 3D field to access and sustain the ELM suppression. At the same time, the 3D-field optimizer adjusts the current distribution across the 3D coils using the output of ML-3D, which guarantees a safe 3D field for disruption avoidance. This model generates the relations between coil currents ($R_{M,B}, \phi_{T,B}$) at every 1 ms given equilibrium state. Figure 4(a-d) illustrates the performance of ML-3D with a randomly selected test discharge, showing good agreement between the offline and ML-3D outputs. A low-pass filter is applied to prevent overly rapid changes in the 3D-coil commands that could result in damage to the coils.

In KSTAR discharge (#31873) with plasma current, $I_p = 0.51$ MA, edge magnetic pitch angle, $q_{95} \sim 5.1$, and ~ 2.5 MW of neutral beam injection heating, the ML-integrated adaptive RMP optimizer is triggered at 4.5 s and successfully achieves fully-automated ELM suppression without the need for pre-programmed waveforms. Shown in Fig. 5a, I_{RMP} starts increasing at 4.5 s with a rate of 3 kA/s to access the

ELM suppression, while $R_{M,B}$ and $\phi_{T,B}$ adjust simultaneously. As a 3D coil setup is automatically optimized by ML-3D during the entire discharge, safe ELM suppression is achieved at 6.2 s.

During the optimization process (see Fig. 5d), ML-3D maintains r_B at a level similar to the empirically optimized 3D setup (standard, $R_{M,B}=1, \phi_{T,B}=\pi/2$). Interestingly, ML-3D achieves such a favorable r_B even with different coil configurations from the empirical (standard) case, highlighting the capability of ML-3D in finding totally new physics-informed path of 3D-field optimization. It is clear that ϵ ($=r_{B,ML}/r_{B,STD}$) stays near or below unity, where $r_{B,ML}$ and $r_{B,STD}$ are r_B from ML-3D and standard setup, respectively. Furthermore, ML-3D performs better than the empirical setup in the early stages of ELM suppression (<6 s), showing much lower r_B than the standard case (or $\epsilon < 1$). This behavior is particularly beneficial as keeping r_B small in the early ELM control phase is key to avoiding disruption, explaining how the successful automated ELM suppression is achieved. Therefore, these results show the 3D-ML as a viable solution for automated ELM-free access. Notably, ML-3D is based on a physics-based model and doesn't require experimental data, making its extension to ITER and future fusion reactors straightforward. This robust applicability to future devices highlights the advantage of the ML-integrated 3D-field optimization scheme. It is worth pointing out that the operational limits of the KSTAR-3D coils are restricting the ML-3D's ability to further optimize r_B in #31873. In future devices with higher current limits for 3D coils, better field optimization and improved fusion performance are expected.

As shown in Fig. 5a, the plasma performance significantly decreases from $G \sim 0.17$ (4 s, before 3D-field application) to $G \sim 0.1$ after the first ELM suppression at 6.2 s, which is the major disadvantage of 3D-field. Here, $G = \beta_N H_{89}/q_{95}^2$ is the figure of merit, β_N is the normalized beta, $H_{89} = \tau_{exp}/\tau_{89}$ is the energy confinement quality compared to the standard tokamak plasmas, τ_{exp} is the experimental energy confinement time, and τ_{89} is the empirically derived confinement time using standard tokamak plasma database³. Following the initial degradation, however, the confinement starts to increase, eventually reaching a converged state by 8.7 s with an enhanced final state of $G \sim 0.16$, reaching the initial high-confinement state. This corresponds to a 60% boost from G in a standard ELM-suppressed state. Such a notable fusion performance boost is an outcome of adaptive amplitude (I_{RMP}) optimization starting at 6.2 s, which will be described in the next section.

Enhanced fusion performance using adaptive optimization. Figure 6 presents a compelling illustration of H-mode plasmas from both DIII-D ($n_{RMP} = 3$) and KSTAR ($n_{RMP} = 1$), effectively achieving fully suppressed ELMs through adaptive feedback RMP amplitude optimization. The RMP-hysteresis from the plasma response is harnessed in these discharges, allowing for sustained ELM suppression with lower RMP strength than initially required to access the ELM suppression regime³⁶. As the RMP amplitude is reduced, the pressure pedestal height increases, leading to

a notable global confinement boost in an ELM-suppressed state. In this section, we employ a pre-set RMP waveform or 3D spectrum and apply real-time feedback to control its amplitude (I_{RMP}). Therefore, the results illustrate the pure effect of adaptive amplitude optimization.

In DIII-D discharge (#190736) with $I_p = 1.62$ MA, $q_{95} \sim 3.35$, and ~ 5.8 MW of neutral beam injection heating, the plasma exhibits initial performance of $G \sim 0.39$ and $H_{89} \sim 2.15$, closely aligned with the target of the ITER baseline scenario, including plasma shape.

However, after the first stable ELM suppression is achieved through conventional RMP-ramp up ($n_{RMP} = 3$), the plasma performance notably decreases to $G \sim 0.18$ and $H_{89} \sim 1.45$. This 54% reduction in G is mainly attributed to the degradation in density and temperature pedestals, as depicted in Fig. 6d,e. Similarly, in the KSTAR discharge with $I_p = 0.51$ MA, $q_{95} \sim 5$, and ~ 3 MW of neutral beam heating, significant performance degradation is observed from $G \sim 0.19$ and $H_{89} \sim 2.24$ to $G \sim 0.11$ and $H_{89} \sim 1.69$ after ELM suppression by $n_{RMP}=1$ RMPs (Fig. 6h). These extensive degradations are a well-known general trend in RMP experiments^{13,37–39}. Such H_{89} and G degradation cannot be accepted in future fusion reactors due to the substantial deviation from the ITER baseline level ($H_{89}=2$, $G=0.4$) and increase in fusion cost.

Following the initial degradation, the real-time adaptive RMP optimization scheme improves fusion performance while maintaining stable ELM suppression. The controller relies on the D_α emission signal near the outer divertor target to monitor the ELM events. To achieve ELM suppression, the RMP amplitude (I_{RMP}) is increased until ELM suppression. Subsequently, during the ensuing ELM-suppressed phase, the controller lowers I_{RMP} to raise the pedestal height until ELMs reappear, at which point the control ramps up the RMP amplitude again to achieve suppression (Fig. 6b). A 0.5 s RMP flat-top interval is introduced between the RMP-ramp up and down phases in the experiment to achieve a saturated RMP response. As mentioned earlier, the 3D shape of RMP is pre-programmed for safe ELM suppression and only adjusts the amplitude.

With the adaptive RMP optimization, the plasma performance of discharge #190736 is enhanced to $G \sim 0.33$ and $H_{89} \sim 2.05$, which corresponds to 83% and 41% improvement of G and H_{89} of standard RMP-ELM suppressed state, respectively. Notably, the increase in G_{fus} is particularly significant, reaching the ITER-relevant level, highlighting the advantage of adaptive optimization. We note that the further performance increase during the *transient* ELM-free period (>2.95 s) with rapid density increase is not considered to avoid overestimating the control performance. The improved confinement quality is attributed to enhanced temperature and density pedestals. As shown in Fig. 6(d,e), all pedestals are improved compared to the initial ELM suppression phase. For example, the electron ($T_{e,ped}$) and ion ($T_{i,ped}$) temperature pedestals increase by 25% and 28%, respectively. The electron density pedestal ($n_{e,ped}$) also shows a 23% increase during the same period.

The strong performance boost is similarly achieved in KSTAR discharge #26004. To leverage the long-pulse feasi-

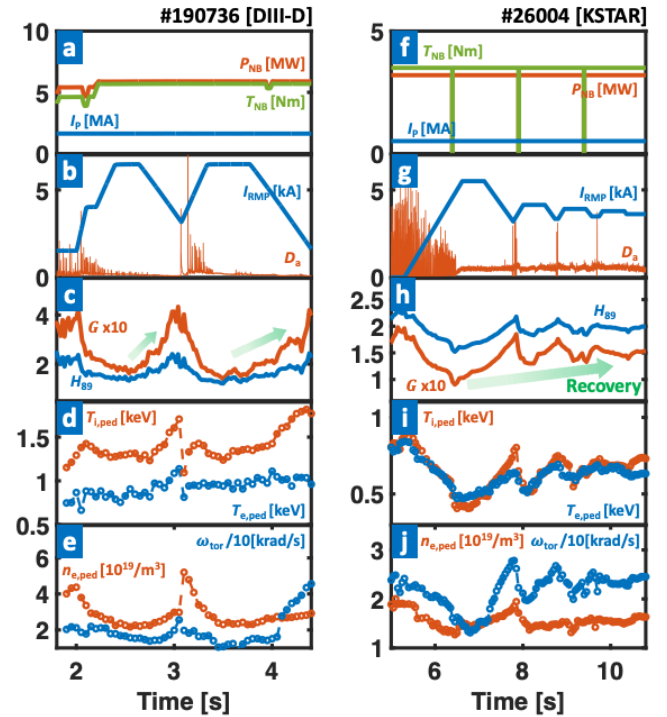


Figure 6. Plasma parameters for an ELM suppression discharges (#190736 [a-e] and #26004 [f-j]) with adaptive amplitude optimization. a,f Plasma current (I_p , blue), NBI heating (P_{NB} , orange), and torque (T_{NB} , green). b,g RMP coil current (I_{RMP} , blue) and D_α emission (orange) near outer divertor target. c,h H_{89} (blue) and G (orange). d,i Pedestal height of electron ($T_{e,ped}$, blue) and ion ($T_{i,ped}$, orange) temperature. e,j Pedestal height of electron density ($n_{e,ped}$, blue) and toroidal rotation frequency of carbon (6+) impurity ($\omega_{tor,ped}$, orange).

bility (>10 s) of KSTAR, the adaptive optimization scheme is implemented with the lower bound of I_{RMP} set slightly higher (by 0.1kA) than where the most recent ELM returns. This adaptive constraint reduces control oscillation and enables the plasma to converge to an operating point after sufficient iterations, optimizing both ELM stability and confinement. In the selected discharge, the adaptive scheme reaches a stable ELM-suppressed phase after 10 s, with enhanced global confinement, as illustrated in Fig. 6(g,h). The plasma performance in this final state shows $G \sim 0.15$ and $H_{89} \sim 1.98$, increasing up to 37% and 17% of G and H_{89} at initial ELM suppression. This successful iteration of the adaptation scheme in longer pulses also supports its applicability in ITER long pulses.

The adaptive scheme has been extensively tested in both tokamaks over 30 discharges with multi-toroidal wave number of RMP (n_{RMP}) of $n_{RMP} = 1 - 2$ (KSTAR) and 3 (DIII-D), demonstrating its robust performance in boosting ELM-suppressed plasma performance. It is noteworthy that ITER-tokamak will utilize high- n ($n_{RMP}=3$) while fusion reactor may rely on low- n due to the engineering limitations⁴⁰. Therefore, it is important to confirm the multi- n capability of the adaptive RMP scheme. As shown in Fig. 7, we observe an

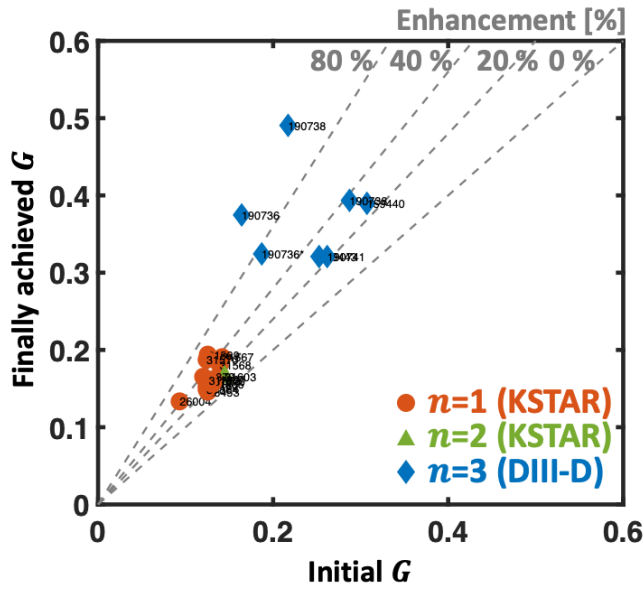


Figure 7. Performance enhancement in discharge with adaptive RMP optimization. G at initial (standard) ELM-suppressed state versus finally achieved G from the initial state by adaptive RMP optimization. The circle (orange), triangle (green), and diamond (blue) dots correspond to $n=1$ (KSTAR), $n=2$ (KSTAR), and $n=3$ (DIII-D) cases, respectively. The dotted grey lines show the degree of G enhancement by the adaptive scheme.

effective G enhancement from the standard ELM-suppressed state regardless of n_{RMP} , affirming the multi- n compatibility of the adaptive RMP optimization for ITER and future fusion reactors. With such success, the ELM-suppressed discharges with RMP optimization perform the best G among the various ELM-free scenarios (see Fig. 2) in DIII-D and KSTAR, including Non-ELM scenarios³⁹ where ELMs are intrinsically suppressed without using 3D-fields. This highlights that adaptive 3D-field optimization is one of the most effective ways to achieve a high-performance ELM-free scenario. Furthermore, the enhanced H_{89} can result in an increased non-inductive current fraction. This improvement reduces the flux consumption in the central solenoid, thereby extending the pulse length. Therefore, the adaptive RMP scheme has contributed to notable ELM-suppression long-pulse records⁴¹ over 45s in KSTAR, which is also an essential advantage for ITER operations. We emphasize that the feasibility of utilizing RMP-hysteresis in a feed-forward approach is restricted. This limitation stems from the challenges in precisely predicting the required RMP strength to achieve and sustain ELM suppression. Notably, such an advantage remains exclusive to the adaptive real-time scheme.

Interestingly, a very high fusion G boost over 80% is observed in the $n_{\text{RMP}} = 3$ results for the DIII-D cases, recovering most of the performance lost by RMP (see Fig. 7). This further highlights the performance of adaptive RMP optimization, a key to accessing ELM-suppressed high-confinement scenarios. We'll revisit the analysis and insights behind these strong performance enhancements in the last part of this paper.

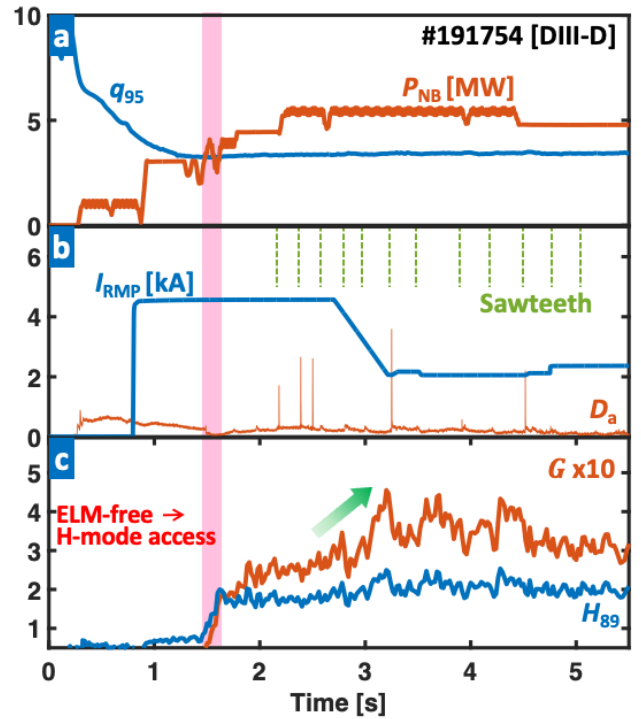


Figure 8. Plasma parameters with an integrated RMP optimization (#191754), reaching near-zero ELMs. **a** q_{95} (blue) and P_{NB} (orange). **b** I_{RMP} (blue) and D_{α} emission (orange) near outer divertor target. **c** H_{89} (blue) and G (orange). The red-colored area highlights the H-mode access without early ELMs. The green dotted lines in **b** show the sawteeth timing.

Nearly complete ELM-free operation with high performance by integrated RMP optimization. It is worth pointing out that the amplitude optimization process results in multiple ELMs before accessing the optimized state. As shown in Fig. 6(b,g), the ELMs reappear during RMP amplitude optimization. These can be considered acceptable as they can be reduced with control tuning, and also, few ELMs are tolerable in future fusion machines. However, avoiding extensive ELMs between the LH transition and the first ELM suppression is vital. Previous research has demonstrated that early RMP-ramp up^{42,43} before the first ELM reduces ELMs during the early H-mode phase. Nevertheless, this approach often faced limitations due to uncertainties in determining the required conditions, including initial RMP amplitude for suppressing the first ELMs. While using a sufficiently large RMP could guarantee early ELM suppression, it leads to poor confinement.

The integration of early RMP and 3D-field optimization schemes provides an effective solution to address these limitations. Figure 8 illustrates a DIII-D discharge (#191754) of near-zero ELMs, where the adaptive RMP optimization is integrated with early RMP ramp-up. Notably, establishing a strong RMP of $I_{\text{RMP}}=4.7$ kA (at 0.8s) successfully suppresses early ELMs, enabling ELM-free access to H-mode. Subsequently, the RMP optimization improves the performance

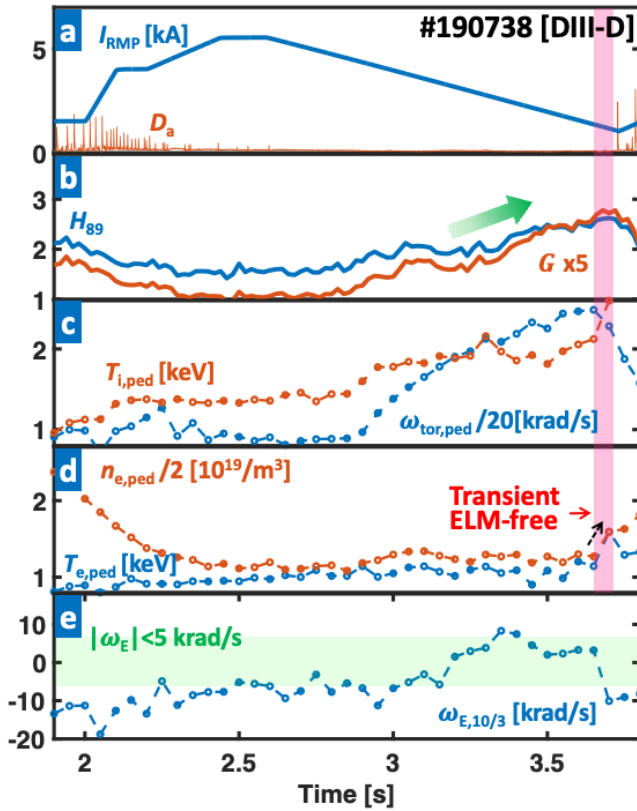


Figure 9. Plasma parameters of an optimized RMP amplitude (#190738) with highly enhanced performance. **a** I_{RMP} (blue) and D_α emission (orange) near the outer divertor target. **b** H_{89} (blue) and G (orange). **c** $\omega_{tor,ped}$ (blue) and $T_{i,ped}$ (orange). **c** $T_{e,ped}$ (blue) and $n_{e,ped}$ (orange). **e** ExB rotation frequency (ω_E) at $q=10/3$ (blue). The red and green colored regions show the transient ELM-free phase and $|\omega_E| < 5$ krad/s, respectively.

from 2.7s, leading to the boost of $G=0.28$ and $H_{89}=1.83$ at standard ELM-suppressed state to $G=0.39$ and $H_{89}=2.18$. Despite the successful integration of optimizing schemes, complete ELM suppression remains challenging due to a few sporadic ELMs induced by sawteeth activity during the ELM suppressed phase, as shown in Fig. 8b. These sporadic ELMs lead the controller to overestimate the ELM instability, thereby hindering further optimizations (or decreases) of the RMP amplitude, ultimately limiting the additional improvement in confinement. Nevertheless, the plasma performance still exceeds the ITER-relevant baseline ($H_{89}=2$), highlighting the benefits of the adaptive scheme. In the future, further progress can be pursued by exploring scenarios with reduced or mitigated sawtooth, potentially leading to even greater improvements in ELM control and optimization performance.

Physics behind on accessing highly enhanced Edge-Energy-Burst-free phase by adaptive optimization. The achievement of the ELM-suppressed state by resonant magnetic perturbation (RMP) is generally understood to be due to field penetration and pedestal gradient reduction. When RMP

is applied externally, the plasma response mainly shields it, and a sufficiently strong amplitude is required to penetrate the plasma and form magnetic islands that cause additional pedestal transport. The plasma flow (ω_E), formed by ExB forces due to electric (E) and magnetic (B) fields, is known to strengthen the RMP shielding effect, causing the amplitude threshold ($I_{RMP,th}$) required to access and maintain the ELM-suppressed state to increase. In particular, it is found that the value of ω_E on the rational surfaces near the electron pedestal top mainly increases $I_{RMP,th}$ because magnetic islands on these surfaces are key to the ELM suppression⁴⁴. Following the penetration of RMPs, the pedestal gradient decreases due to RMP-induced transport, and ELM suppression is attained once the gradient falls below the ELM stability limit. In theory, the pressure gradient at the pedestal center should stay under the stability limit to avoid the reappearance of ELMs⁴⁵. Here, this gradient reduction results in a decrease in pedestal height and global confinement. Considering these factors, strict control boundaries exist for the RMP amplitude and pedestal gradient to ensure stable ELM suppression. These limitations often constrain the strong confinement to boost through adaptive RMP optimization. Remarkably, however, the highly optimized cases exhibiting more than an 80% G enhancement, as shown in Figure 7, offer an insight to overcome limitations in a performance boost.

Figure 9 shows an ELM-suppressed discharge in DIII-D (#190738), which achieves $>80\%$ G enhancement by adaptive $n=3$ RMP optimization. After the first stable ELM suppression at 2.45s with $I_{RMP}=5.4$ kA, the plasma performance improves from $G \sim 0.22$ and $H_{89} \sim 1.58$ up to $G \sim 0.49$ and $H_{89} \sim 2.42$ at 3.55s. This significant performance boost is characterized by a gradual change that differs from the transient confinement increase typically observed in *transient* ELM-free periods (>3.7 s) in that a sharp increase in density pedestal is not observed before 3.65 s. In these highly enhanced states, the ELM suppression is maintained until $I_{RMP} \sim 1.5$ kA, exhibiting more than 70% of RMP-hysteresis, as shown in Fig. 9a, which dramatically exceeds typical values ($\sim 40\%$) in other cases⁴⁶. Because a smaller RMP amplitude means higher performance, such a strong hysteresis is the main contributor to performance enhancement.

The strong RMP-hysteresis observed in this experiment is correlated with the self-consistent evolution of the plasma flow in the RMP control. As shown in Fig. 9c, the toroidal rotation at the pedestal top ($\omega_{tor,ped}$) increases as the RMP decreases. Then, the increase in $\omega_{tor,ped}$ alters the momentum balance of the plasma, causing $\omega_{E,10/3}$ to decrease toward zero in the electron pedestal top region, located at the $q=10/3$ rational surface. Figure 9(c,e) shows this correlation between increasing $\omega_{tor,ped}$ and $\omega_{E,10/3} \rightarrow 0$. As a result, $I_{RMP,th}$ is relaxed, and the RMP amplitude can be further reduced. Here, an additional decrease in RMP weakens the rotation damping by the 3D field, resulting in a further increase in $\omega_{tor,ped}$, and allows $\omega_{E,10/3}$ and $I_{RMP,th}$ to decrease favorably once again. This synergy between $I_{RMP,th}$ and $\omega_{tor,ped}$ is key to maintaining ELM suppression with very low RMP, leading to a strong confinement enhancement (and rotation), as shown in Fig. 9(a-d). The ELM suppression (~ 4.2 s) in Fig. 6a with

a very low RMP (1.5 kA) also shares the same feature. We note that achieving such a reinforced RMP-induced hysteresis is not trivial in the experiment, requiring pre-programmed and dedicated RMP waveforms. In this respect, adaptive RMP optimization is an effective methodology, as it can automatically generate and utilize the hysteresis without manual intervention.

The enhanced RMP-hysteresis and rotation increase observed in the experiments also offer promising aspects for future fusion devices. Maintaining thermal and energetic particle confinements in a fusion reactor is essential for achieving high fusion G . However, the presence of RMPs leads to undesired perturbed fields in the core region that adversely affect the fast ion confinement. Additionally, RMP-induced rotation damping poses a critical challenge for ITER, where externally driven torque may not be sufficient to suppress core instabilities and turbulent transport. The strengthened RMP-hysteresis and rotation boost during adaptive RMP optimization can significantly mitigate these unfavorable aspects of RMPs by enabling ELM suppression with very low RMP amplitudes. By reducing the negative impacts of RMPs on fast ion and core confinements, the prospects of an adaptive scheme for achieving high fusion G within future fusion devices become more favorable.

It is noteworthy that the $\omega_{\text{tor,ped}}$ increase in the early RMP-ramp down phase still leaves a question. This may simply be due to the reduced damping caused by the 3D fields^{47,48}. However, the increase in $\omega_{\text{tor,ped}}$ starts 0.3 s later than the 2.6 s that RMP-ramp down starts. This delayed response may indicate that additional mechanisms, such as field penetration or turbulence, are participating in the rotation response. In fact, the change in turbulence along with rotation change is also observed in the experiment. Future studies on plasma rotation in the presence of RMPs will provide further insight into the projection of the RMP-ELM scenario onto ITER and future devices.

II. DISCUSSION

We have successfully optimized controlled ELM-free states with highly enhanced fusion performance in the KSTAR and DIII-D devices, covering low- n RMPs relevant for future reactors to ITER-relevant $n=3$ RMPs and achieving the highest fusion among various ELM-free scenarios in both machines. Furthermore, the innovative integration of the ML algorithm with RMP control enables fully automated 3D-field optimization and ELM-free operation for the first time with strong performance enhancement, supported by an adaptive optimization process. This adaptive approach exhibits compatibility between RMP ELM suppression and high confinement. Additionally, it provides a robust strategy for achieving stable ELM suppression in long-pulse scenarios⁴¹ (lasting more than 45 seconds) by minimizing the loss of confinement and non-inductive current fraction⁴⁹. Notably, a remarkable performance (G) boost is observed in DIII-D with $n=3$ RMPs, showing over a 90% increase from the initial standard ELM-

suppressed state. This enhancement isn't solely attributed to adaptive RMP control but also to the self-consistent evolution of plasma rotation. This response enables ELM suppression with very low RMP amplitudes, leading to enhanced pedestal. This feature is a good example of a system that transitions to an optimal state through a self-organized response to adaptive modulation. In addition, the adaptive scheme is integrated with early RMP-ramp methods, achieving an ITER-relevant ELM-free scenario with nearly complete ELM-free operation. These results confirm that the integrated adaptive RMP control is a highly promising approach for optimizing the ELM-suppressed state, potentially addressing one of the most formidable challenges in achieving practical and economically viable fusion energy.

However, there are remaining features to be improved for a "complete" adaptive RMP optimization. The present strategy, relying on ELM detection, unavoidably encounters several ELMs during the optimization process. This drawback is unfavorable for fusion reactors, where any potential risks must be minimized. Earlier research⁴⁶ has revealed a "precursor pattern" in D_α and turbulence signals, emerging about 20 ms ahead of ELM reappearances during the suppression phase. This distinctive pattern can be harnessed in real-time to prevent ELM reappearance by initiating early RMP actions upon precursor detection, ultimately achieving a genuinely ELM-free optimization. As an extension of these findings, this concept has been successfully demonstrated in KSTAR⁵⁰ by using precursors in D_α signals, leading to nearly complete ELM suppression by monitoring the precursors. In future work, enhanced ELM control performance will be enabled through advanced ELM-loss precursor detection methods incorporating real-time high-frequency fluctuation measurements.

Lastly, achieving robust access to H-mode without ELMs is a non-trivial task. Here, it turns out that the stable q_{95} control within the ELM suppression window before the RMP ramp is key, as shown in Fig. 8a. This significance is demonstrated by achieving more than ten sequential discharges with ELM-free H-mode transitions via delicate q_{95} tailoring. However, the early RMP ramp required for achieving complete ELM suppression might potentially affect the H-mode access by raising the LH-transition threshold⁵¹⁻⁵⁶. This concern must be addressed through fine-tuned early heating and RMP ramp timings to minimize their effect on robust LH transition⁴³. The future integration of these features will be expanding operational flexibility, enhancing fusion performance boost, and developing advanced ELM control techniques for ITER and future tokamaks.

III. METHODS

DIII-D tokamak. The DIII-D tokamak is the largest operating national tokamak device in U.S.A. The reference discharge has the plasma major radius $R_0 = 1.68$ m, minor radius $a_0 = 0.59$ m, and the toroidal magnetic field $B_T = 1.92$ T at major radius R_0 . The $n = 3$ RMP ELM suppression discharge is reproduced with a plasma shape

having elongation $\kappa \sim 1.81$, upper triangularity $\delta_{\text{up}} \sim 0.35$, and lower triangularity $\delta_{\text{low}} \sim 0.69$.

KSTAR tokamak. The KSTAR tokamak is the largest magnetic fusion device in the Republic of Korea, supported by the Korea Institute of Fusion Energy (KFE) and Government funds. The reference discharge has the plasma major radius $R_0 = 1.8$ m, minor radius $a_0 = 0.45$ m, and the toroidal magnetic field $B_T = 1.8$ T at major radius R_0 . The $n = 1$ RMP ELM suppression discharge on KSTAR can be reproduced with a plasma shape having elongation $\kappa \sim 1.71$, upper triangularity $\delta_{\text{up}} \sim 0.37$, and lower triangularity $\delta_{\text{low}} \sim 0.85$.

ELM-free database. The ELM-free database in DIII-D tokamak comes from Ref.³⁹. Here, the previous database uses 300 ms time averaging, while the data point of discharge with adaptive RMP optimization uses a shorter time scale (100 ms) to capture the performance variation with adaptive RMP optimization. The KSTAR database is also constructed using the same process.

Ideal plasma response calculation. The perturbed radial fields (δB_r) from an ideal plasma response by RMP are calculated using GPEC code³² under given magnetic equilibria and 3D coil configuration. The core (B_{core}) and edge (B_{edge}) responses are derived through radially averaging δB_r at $\psi_N = 0 - 0.9$ and $0.9 - 1.0$, respectively. The optimal 3D coil configurations (R_M, R_B, ϕ_T, ϕ_B) of the edge-localized-RMP (ERMP) model are derived using calculated perturbed fields.

Surrogate 3D model. The surrogate model is developed using the dense layer model within the Keras library. The hidden neurons are equipped with ReLU activation function, and they are organized in two layers with 40 and 10 neurons, respectively. In order to train this model, we collected data from 8490 KSTAR time slices in the past three years. The data was split randomly into 6790 and 1700 samples for training and testing the model. In total, this MLP consists of 800 trainable parameters (connection weights), and the training iterations continue for 150 epochs or if the error rates converge. The final R2 score on the test set is 0.91.

Kinetic profile and equilibria reconstruction. Core ion temperature is measured by charge exchange recombination system^{57,58} for Carbon (6+) impurities at outboard mid-plane. Core electron temperature and density are measured by the Thomson Scattering system⁵⁹⁻⁶¹. To obtain well-resolved profiles, the data are averaged over 50 ms. The pedestal height is obtained from hyperbolic tangent fits with edge profiles. Kinetic equilibria are reconstructed for the plasma transport and stability analysis. This equilibrium is calculated from the magnetic reconstruction using EFIT code⁶² with the reconstructed radial profiles. The OMFIT package^{63,64} is used to achieve well-converged equilibrium with automated iteration processes.

Plasma fluctuation measurements. In this work, edge n_e fluctuations are measured from the doppler backscattering

system (DBS)⁶⁵. Here, the measured density fluctuation captures the ion-scale turbulence $k_y \rho_s = 0.3 - 1.5$, rotating in the electron direction, where k_y is the bi-normal wave number, $\rho_s = \sqrt{2m_i T_e} / eB$ is the hybrid Larmor radius, and m_i is deuterium mass.

IV. ACKNOWLEDGMENTS

The authors would like to express their deepest gratitude to KSTAR and the DIII-D team. This material was supported by the U.S. Department of Energy, under Awards DE-SC0020372, DE-AC52-07NA27344, DE-AC05-00OR22725, DE-SC0022270, DE-SC0022272, and DE-SC0019352. The U.S. Department of Energy also supported this work under contract number DEAC02-09CH11466 (Princeton Plasma Physics Laboratory). The United States Government retains a non-exclusive, paidup, irrevocable, worldwide license to publish or reproduce the published form of this manuscript or allow others to do so for United States Government purposes. This material is based upon work supported by the U.S. Department of Energy, Office of Science, Office of Fusion Energy Sciences, using the DIII-D National Fusion Facility, a DOE Office of Science user facility, under Award(s) DE-FC02-04ER54698. This research was also supported by R&D Program of "KSTAR Experimental Collaboration and Fusion Plasma Research(EN2301-14)" through the Korea Institute of Fusion Energy(KFE), funded by the Government funds. **Disclaimer:** This report was prepared as an account of work sponsored by an agency of the United States Government. Neither the United States Government nor any agency thereof, nor any of their employees, makes any warranty, express or implied, or assumes any legal liability or responsibility for the accuracy, completeness, or usefulness of any information, apparatus, product, or process disclosed, or represents that its use would not infringe privately owned rights. Reference herein to any specific commercial product, process, or service by trade name, trademark, manufacturer, or otherwise does not necessarily constitute or imply its endorsement, recommendation, or favoring by the United States Government or any agency thereof. The views and opinions of authors expressed herein do not necessarily state or reflect those of the United States Government or any agency thereof.

V. AUTHOR CONTRIBUTIONS

S.K., R.S., S.Y. led the control development, experimental demonstration, and analysis. E.K. conceived the original idea of adaptive control. Q.H. gave and shared the fundamental guidance of the experimental plan and analysis. A.O.N. analyzed the micro instability with Gyro-kinetic code. S.H., R.W., N.L., Y.J., M.K., and A.B. supported the experimental procedures. R.N. and C.P.S. discussed the critical physics picture of transports at the pedestal. J.P. and N.L. discussed the role of RMP response, stability, and transport analysis of the pedestal region. H.R., T.R., W.K., and J.L. analyzed the profile and fluctuation measurements. A.J. supported the de-

velopment of the surrogate model. Y.N., A.B., and J.S. advise the scope of the experimental analysis. S.K. wrote the main manuscript text, and A.O.N. and all authors reviewed it.

VI. ADDITIONAL INFORMATION

Competing financial interests: The authors declare no competing financial interests.

REFERENCES

- ¹C. Gormezano, A. Sips, T. Luce, S. Ide, A. Becoulet, X. Litaudon, A. Isayama, J. Hobirk, M. Wade, T. Oikawa, R. Prater, A. Zvonkov, B. Lloyd, T. Suzuki, E. Barbato, P. Bonoli, C. Phillips, V. Vdovin, E. Joffrin, T. Casper, J. Ferron, D. Mazon, D. Moreau, R. Bundy, C. Kessel, A. Fukuyama, N. Hayashi, F. Imbeaux, M. Murakami, A. Polevoi, and H. S. John, "Chapter 6: Steady state operation," *Nuclear Fusion* **47**, S285–S336 (2007).
- ²A. Peeters, C. Angioni, and A. Sips, "On the extrapolation to ITER of discharges in present tokamaks," *Nuclear Fusion* **47**, 1341–1345 (2007).
- ³P. Yushmanov, T. Takizuka, K. Riedel, O. Kardaun, J. Cordey, S. Kaye, and D. Post, "Scalings for tokamak energy confinement," *Nuclear Fusion* **30**, 1999–2006 (1990).
- ⁴H. Han, S. J. Park, C. Sung, J. Kang, Y. H. Lee, J. Chung, T. S. Hahn, B. Kim, J.-K. Park, J. G. Bak, M. S. Cha, G. J. Choi, M. J. Choi, J. Gwak, S. H. Hahn, J. Jang, K. C. Lee, J. H. Kim, S. K. Kim, W. C. Kim, J. Ko, W. H. Ko, C. Y. Lee, J. H. Lee, J. H. Lee, J. K. Lee, J. P. Lee, K. D. Lee, Y. S. Park, J. Seo, S. M. Yang, S. W. Yoon, and Y.-S. Na, "A sustained high-temperature fusion plasma regime facilitated by fast ions," *Nature* **609**, 269–275 (2022).
- ⁵F. Wagner, G. Fussmann, T. Grave, M. Keilhacker, M. Kornherr, K. Lackner, K. McCormick, E. R. Müller, A. Stäbler, G. Becker, K. Bernhardt, U. Ditte, A. Eberhagen, O. Gehre, J. Gernhardt, G. v. Gierke, E. Glock, O. Gruber, G. Haas, M. Hesse, G. Janeschitz, F. Karger, S. Kissel, O. Klüber, G. Lisitano, H. M. Mayer, D. Meisel, V. Mertens, H. Murmann, W. Poschenrieder, H. Rapp, H. Röhr, F. Ryter, F. Schneider, G. Siller, P. Smeulders, F. Söldner, E. Speth, K. H. Steuer, Z. Szymanski, and O. Vollmer, "Development of an Edge Transport Barrier at the H-Mode Transition of ASDEX," *Physical Review Letters* **53**, 1453–1456 (1984).
- ⁶J. W. Connor, R. J. Hastie, H. R. Wilson, and R. L. Miller, "Magnetohydrodynamic stability of tokamak edge plasmas," *Physics of Plasmas* **5**, 2687–2700 (1998).
- ⁷A. Loarte, G. Huijsmans, S. Futatani, L. Baylor, T. Evans, D. M. Orlov, O. Schmitz, M. Becoulet, P. Cahyna, Y. Gribov, A. Kavin, A. Sashala Naik, D. Campbell, T. Casper, E. Daly, H. Frerichs, A. Kischner, R. Laengner, S. Lisgo, R. Pitts, G. Saibene, and A. Wingen, "Progress on the application of ELM control schemes to ITER scenarios from the non-active phase to DT operation," *Nuclear Fusion* **54**, 033007 (2014).
- ⁸J. Gunn, S. Carpentier-Chouchana, F. Escourbiac, T. Hirai, S. Panayotis, R. Pitts, Y. Corre, R. Dejarnac, M. Firdaouss, M. Kočan, M. Komm, A. Kukushkin, P. Languille, M. Missirlian, W. Zhao, and G. Zhong, "Surface heat loads on the ITER divertor vertical targets," *Nuclear Fusion* **57**, 046025 (2017).
- ⁹I. P. E. G. o. C. Transport, I. P. E. G. o. C. Database, and I. P. B. Editors, "Chapter 2: Plasma confinement and transport," *Nuclear Fusion* **39**, 2175–2249 (1999).
- ¹⁰T. E. Evans, R. A. Moyer, K. H. Burrell, M. E. Fenstermacher, I. Joseph, A. W. Leonard, T. H. Osborne, G. D. Porter, M. J. Schaffer, P. B. Snyder, P. R. Thomas, J. G. Watkins, and W. P. West, "Edge stability and transport control with resonant magnetic perturbations in collisionless tokamak plasmas," *Nature Physics* **2**, 419–423 (2006).
- ¹¹W. Suttrop, T. Eich, J. C. Fuchs, S. Günter, A. Janzer, A. Herrmann, A. Kallenbach, P. T. Lang, T. Lunt, M. Maraschek, R. M. McDermott, A. Mlynek, T. Pütterich, M. Rott, T. Vierle, E. Wolftrum, Q. Yu, I. Zammutto, and H. Zohm, "First Observation of Edge Localized Modes Mitigation with Resonant and Nonresonant Magnetic Perturbations in ASDEX Upgrade," *Physical Review Letters* **106**, 225004 (2011).
- ¹²Y. M. Jeon, J.-K. Park, S. W. Yoon, W. H. Ko, S. G. Lee, K. D. Lee, G. S. Yun, Y. U. Nam, W. C. Kim, J.-G. Kwak, K. S. Lee, H. K. Kim, and H. L. Yang, "Suppression of Edge Localized Modes in High-Confinement KSTAR Plasmas by Nonaxisymmetric Magnetic Perturbations," *Physical Review Letters* **109** (2012), 10.1103/physrevlett.109.035004.
- ¹³Y. Sun, Y. Liang, Y. \. e. Liu, S. Gu, X. Yang, W. Guo, T. Shi, M. Jia, L. Wang, B. Lyu, C. Zhou, A. Liu, Q. Zang, H. Liu, N. Chu, H. \. e. Wang, T. Zhang, J. Qian, L. Xu, K. He, D. Chen, B. Shen, X. Gong, X. Ji, S. Wang, M. Qi, Y. Song, Q. Yuan, Z. Sheng, G. Gao, P. Fu, and B. Wan, "Nonlinear Transition from Mitigation to Suppression of the Edge Localized Mode with Resonant Magnetic Perturbations in the EAST Tokamak," *Physical Review Letters* **117** (2016), 10.1103/physrevlett.117.115001.
- ¹⁴M. E. Fenstermacher, T. E. Evans, T. H. Osborne, M. J. Schaffer, M. P. Aldan, J. S. deGrassie, P. Gohil, I. Joseph, R. A. Moyer, P. B. Snyder, R. J. Groebner, M. Jakubowski, A. W. Leonard, O. Schmitz, and the DIII-D Team, "Effect of island overlap on edge localized mode suppression by resonant magnetic perturbations in DIII-D," *Physics of Plasmas* **15**, 056122 (2008).
- ¹⁵V. Rozhansky, E. Kaveeva, P. Molchanov, I. Veselova, S. Voskoboinikov, D. Coster, A. Kirk, S. Lisgo, and E. Nardon, "Modification of the edge transport barrier by resonant magnetic perturbations," *Nuclear Fusion* **50**, 034005 (2010).
- ¹⁶R. Nazikian, C. Paz-Soldan, J. Callen, J. deGrassie, D. Eldon, T. Evans, N. Ferraro, B. Grierson, R. Groebner, S. Haskey, C. Hegna, J. King, N. Logan, G. McKee, R. Moyer, M. Okabayashi, D. Orlov, T. Osborne, J.-K. Park, T. Rhodes, M. Shafer, P. Snyder, W. Solomon, E. Strait, and M. Wade, "Pedestal Bifurcation and Resonant Field Penetration at the Threshold of Edge-Localized Mode Suppression in the DIII-D Tokamak," *Physical Review Letters* **114**, 105002 (2015).
- ¹⁷C. Paz-Soldan, R. Nazikian, S. Haskey, N. Logan, E. Strait, N. Ferraro, J. Hanson, J. King, M. Lanctot, R. Moyer, M. Okabayashi, J.-K. Park, M. Shafer, and B. Tobias, "Observation of a Multimode Plasma Response and its Relationship to Density Pumpout and Edge-Localized Mode Suppression," *Physical Review Letters* **114**, 105001 (2015).
- ¹⁸Q. M. Hu, R. Nazikian, B. A. Grierson, N. C. Logan, J.-K. Park, C. Paz-Soldan, and Q. Yu, "The density dependence of edge-localized-mode suppression and pump-out by resonant magnetic perturbations in the DIII-D tokamak," *Physics of Plasmas* **26**, 120702 (2019), publisher: AIP Publishing.
- ¹⁹R. Fitzpatrick, "Theory of edge localized mode suppression by static resonant magnetic perturbations in the DIII-D tokamak," *Physics of Plasmas* **27**, 042506 (2020).
- ²⁰Y. Liu, C. Paz-Soldan, L. Li, and Y. Sun, "Role of 3D neoclassical particle flux in density pump-out during ELM control by RMP in DIII-D," *Nuclear Fusion* **60**, 036018 (2020).
- ²¹S. Mordijck, R. A. Moyer, and G. R. McKee, "Changes in density fluctuations as a result of resonant magnetic perturbations correlate with the density inverse scale length," *Physics of Plasmas* **19**, 024504 (2012).
- ²²G. McKee, Z. Yan, C. Holland, R. Buttery, T. Evans, R. Moyer, S. Mordijck, R. Nazikian, T. Rhodes, O. Schmitz, and M. Wade, "Increase of turbulence and transport with resonant magnetic perturbations in ELM-suppressed plasmas on DIII-D," *Nuclear Fusion* **53**, 113011 (2013).
- ²³H. Müller, T. Lunt, W. Suttrop, T. Eich, R. Fischer, J. Fuchs, A. Herrmann, M. Kočan, P. de Maré, and E. Wolftrum, "Modification of scrape-off layer transport and turbulence by non-axisymmetric magnetic perturbations in ASDEX Upgrade," *Journal of Nuclear Materials* **438**, S64–S71 (2013).
- ²⁴S. Liu, N. Yan, Y. Liang, H. Zhang, J. Xu, G. Xu, L. Wang, R. Chen, G. Hu, Y. Ye, Y. Sun, T. Shi, H. Wang, M. Wu, X. Wu, S. Gu, M. Jia, N. Chu, Q. Ma, Y. Wang, T. Zhang, X. Han, L. Chen, J. Liu, S. Xu, H. Wang, N. Zhao, W. Zhang, J. Qian, L. Zeng, L. Xu, S. Wang, H. Liu, Q. Zang, Y. Yu, L. Liao, X. Gong, and EAST, "Edge turbulence characteristics and transport during the ELM mitigation with $n = 1$ resonant magnetic perturbation on EAST," *Nuclear Fusion* **60**, 082001 (2020).
- ²⁵P. Snyder, K. Burrell, H. Wilson, M. Chu, M. Fenstermacher, A. Leonard, R. Moyer, T. Osborne, M. Umansky, W. West, and X. Xu, "Stability and dynamics of the edge pedestal in the low collisionality regime: physics mechanisms for steady-state ELM-free operation," *Nuclear Fusion* **47**, 961–968 (2007).

- ²⁶F. Laggner, D. Eldon, A. Nelson, C. Paz-Soldan, A. Bortolon, T. Evans, M. Fenstermacher, B. Grierson, Q. Hu, D. Humphreys, A. Hyatt, R. Nazikian, O. Meneghini, P. Snyder, E. Unterberg, E. Kolemen, and t. DIII-D team, "Real-time pedestal optimization and ELM control with 3D fields and gas flows on DIII-D," *Nuclear Fusion* **60**, 076004 (2020).
- ²⁷R. Shousha, S. K. Kim, K. G. Erickson, S. H. Hahn, A. O. Nelson, S. M. Yang, J.-K. Park, J. Wai, Y. M. Jeon, J. H. Lee, J. Jang, D. Seo, and E. Kolemen, "Design and experimental demonstration of feedback adaptive RMP ELM controller toward complete long pulse ELM suppression on KSTAR," *Physics of Plasmas* **29**, 032514 (2022).
- ²⁸J. Kates-Harbeck, A. Svyatkovskiy, and W. Tang, "Predicting disruptive instabilities in controlled fusion plasmas through deep learning," *Nature* **568**, 526–531 (2019).
- ²⁹J. Degraeve, F. Felici, J. Buchli, M. Neunert, B. Tracey, F. Carpanese, T. Ewalds, R. Hafner, A. Abdolmaleki, D. de las Casas, C. Donner, L. Fritz, C. Galperti, A. Huber, J. Keeling, M. Tsimpoukelli, J. Kay, A. Merle, J.-M. Moret, S. Noury, F. Pesamosca, D. Pfau, O. Sauter, C. Sommariva, S. Coda, B. Duval, A. Fasoli, P. Kohli, K. Kavukcuoglu, D. Hassabis, and M. Riedmiller, "Magnetic control of tokamak plasmas through deep reinforcement learning," *Nature* **602**, 414–419 (2022).
- ³⁰J. Vega, A. Murari, S. Dormido-Canto, G. A. Rattá, M. Gelfusa, and JET Contributors, "Disruption prediction with artificial intelligence techniques in tokamak plasmas," *Nature Physics* **18**, 741–750 (2022).
- ³¹S. Yang, J.-K. Park, Y. Jeon, N. Logan, J. Lee, Q. Hu, S. Lee, J.H. Kim, J. Kim, Y. Na, T. Hahn, and G. Choi, "Tailoring tokamak error fields to control plasma instabilities and transport," *Nature communications*, accepted (2023).
- ³²J.-k. Park, A. H. Boozer, and A. H. Glasser, "Computation of three-dimensional tokamak and spherical torus equilibria," *Physics of Plasmas* **14**, 052110 (2007).
- ³³J.-K. Park, Y. Jeon, Y. In, J.-W. Ahn, R. Nazikian, G. Park, J. Kim, H. Lee, W. Ko, H.-S. Kim, N. C. Logan, Z. Wang, E. A. Feibush, J. E. Menard, and M. C. Zarnstorff, "3D field phase-space control in tokamak plasmas," *Nature Physics* **14**, 1223–1228 (2018).
- ³⁴J.-K. Park, S. Yang, N. Logan, Q. Hu, C. Zhu, M. Zarnstorff, R. Nazikian, C. Paz-Soldan, Y. Jeon, and W. Ko, "Quasisymmetric Optimization of Non-axisymmetry in Tokamaks," *Physical Review Letters* **126**, 125001 (2021).
- ³⁵J. Ferron, M. Walker, L. Lao, H. S. John, D. Humphreys, and J. Leuer, "Real-time equilibrium reconstruction for tokamak discharge control," *Nuclear Fusion* **38**, 1055–1066 (1998).
- ³⁶R. Nazikian, E. Eldon, T. Evans, N. Ferraro, B. Grierson, and R. Groebner, "Advances in the understanding of elm suppression by resonant magnetic perturbations (rmps) in diiii-d and implications for iter," in *25th IAEA Fusion Energy Conference (FEC 2014)* (2014).
- ³⁷W. Suttrop, A. Kirk, R. Nazikian, N. Leuthold, E. Strumberger, M. Wilensdorfer, M. Cavedon, M. Dunne, R. Fischer, S. Fietz, J. C. Fuchs, Y. Q. Liu, R. M. McDermott, F. Orain, D. A. Ryan, E. Viezzer, and a. and, "Experimental studies of high-confinement mode plasma response to non-axisymmetric magnetic perturbations in ASDEX Upgrade," *Plasma Physics and Controlled Fusion* **59**, 014049 (2016), publisher: IOP Publishing.
- ³⁸M. Kim, J. Lee, W. H. Ko, S.-H. Hahn, Y. In, Y. M. Jeon, W. Suttrop, S. K. Kim, G. Y. Park, J.-W. Juhn, and J. H. Lee, "Pedestal electron collisionality and toroidal rotation during ELM-crash suppression phase under $n = 1$ RMP in KSTAR," *Physics of Plasmas* **27**, 112501 (2020).
- ³⁹C. Paz-Soldan, "Plasma performance and operational space without ELMs in DIII-D," *Plasma Physics and Controlled Fusion* **63**, 083001 (2021).
- ⁴⁰S. Yang, J.-K. Park, N. Logan, C. Zhu, Q. Hu, Y. Jeon, Y. In, W. Ko, S. Kim, Y. Lee, and Y. Na, "Localizing resonant magnetic perturbations for edge localized mode control in KSTAR," *Nuclear Fusion* **60**, 096023 (2020).
- ⁴¹J.-K. Park, S. Kim, S. Yang, Q. Hu, J. Snipes, G. W. Shin, M. W. Kim, H. S. Han, Y. M. Jeon, H.-S. Kim, T. Rhee, G. Park, W. H. Ko, J. H. Lee, J. W. Juhn, R. Shousha, E. Kolemen, N. Logan, and C. Paz-Soldan, "Progress towards elm-less h-mode operations in kstar long pulses with resonant magnetic perturbations," in *29th IAEA Fusion Energy Conference (FEC 2023)* (2023).
- ⁴²T. E. Evans and the DIII-D Team, "Suppression and Mitigation of Edge Localized Modes in the DIII-D Tokamak with 3D Magnetic Perturbations," *Plasma and Fusion Research* **7**, 2402046–2402046 (2012).
- ⁴³G. Shin, H. Han, M. Kim, S.-H. Hahn, W. Ko, G. Park, Y. Lee, M. Lee, M. Kim, J.-W. Juhn, D. Seo, J. Jang, H. Kim, J. Lee, and H. Kim, "Pre-emptive RMP-driven ELM crash suppression automated by a real-time machine-learning classifier in KSTAR," *Nuclear Fusion* **62**, 026035 (2022).
- ⁴⁴Q. Hu, R. Nazikian, B. Grierson, N. Logan, D. Orlov, C. Paz-Soldan, and Q. Yu, "Wide Operational Windows of Edge-Localized Mode Suppression by Resonant Magnetic Perturbations in the DIII-D Tokamak," *Physical Review Letters* **125**, 045001 (2020).
- ⁴⁵Q. M. Hu, R. Nazikian, N. C. Logan, J.-K. Park, C. Paz-Soldan, S. M. Yang, B. A. Grierson, Y. In, Y. M. Jeon, M. Kim, S. K. Kim, D. M. Orlov, G. Y. Park, and Q. Yu, "Predicting operational windows of ELMs suppression by resonant magnetic perturbations in the DIII-D and KSTAR tokamaks," *Physics of Plasmas* **28**, 052505 (2021).
- ⁴⁶S. Kim, R. Shousha, S. Hahn, A. Nelson, J. Wai, S. Yang, J.-K. Park, R. Nazikian, N. Logan, Y. Jeon, Y. In, J. Lee, J. Kim, C. Lee, Y.-S. Na, and E. Kolemen, "Optimization of 3D controlled ELM-free state with recovered global confinement for KSTAR with $n = 1$ resonant magnetic field perturbation," *Nuclear Fusion* **62**, 026043 (2022).
- ⁴⁷N. C. Logan, J.-K. Park, K. Kim, Z. Wang, and J. W. Berkery, "Neoclassical toroidal viscosity in perturbed equilibria with general tokamak geometry," *Physics of Plasmas* **20**, 122507 (2013).
- ⁴⁸J.-K. Park and N. C. Logan, "Self-consistent perturbed equilibrium with neoclassical toroidal torque in tokamaks," *Physics of Plasmas* **24**, 032505 (2017), publisher: AIP Publishing.
- ⁴⁹M. Kim, G. Shin, J. Lee, W. Ko, H. Hahn, S.-H. Hahn, S. Kim, S. Yang, R. Shousha, H.-S. Kim, J.-W. Juhn, G. Park, and E. Kolemen, "Integrated RMP-based ELM-crash-control process for plasma performance enhancement during ELM crash suppression in KSTAR," *Nuclear Fusion* (2023), 10.1088/1741-4326/ace460.
- ⁵⁰R. Shousha, S. KIM, K. ERICKSON, J.-K. PARK, S. YANG, A. NELSON, and N. LOGAN, "Closed loop rmp elm suppression with minimized confinement degradation using adaptive control demonstrated," in *29th IAEA Fusion Energy Conference (FEC 2023)* (2023).
- ⁵¹A. Leonard, A. Howald, A. Hyatt, T. Shoji, T. Fujita, M. Miura, N. Suzuki, S. Tsuji, and JFT-2M Group, "Effects of applied error fields on the H-mode power threshold of JFT-2M," *Nuclear Fusion* **31**, 1511–1518 (1991).
- ⁵²S. Kaye, R. Maingi, D. Battaglia, R. Bell, C. Chang, J. Hosea, H. Kugel, B. LeBlanc, H. Meyer, G. Park, and J. Wilson, "L-H threshold studies in NSTX," *Nuclear Fusion* **51**, 113019 (2011).
- ⁵³P. Gohil, T. Evans, M. Fenstermacher, J. Ferron, T. Osborne, J. Park, O. Schmitz, J. Scoville, and E. Unterberg, "L-H transition studies on DIII-D to determine H-mode access for operational scenarios in ITER," *Nuclear Fusion* **51**, 103020 (2011).
- ⁵⁴F. Rytter, S. Rathgeber, E. Viezzer, W. Suttrop, A. Burckhart, R. Fischer, B. Kurzan, S. Potzel, and T. Pütterich, "L-H transition in the presence of magnetic perturbations in ASDEX Upgrade," *Nuclear Fusion* **52**, 114014 (2012).
- ⁵⁵Y. In, J.-K. Park, Y. M. Jeon, J. Kim, G. Y. Park, J.-W. Ahn, A. Loarte, W. H. Ko, H. H. Lee, J. W. Yoo, J. W. Juhn, S. W. Yoon, and H. P. and, "Enhanced understanding of non-axisymmetric intrinsic and controlled field impacts in tokamaks," *Nuclear Fusion* **57**, 116054 (2017), publisher: IOP Publishing.
- ⁵⁶L. Schmitz, D. Kriete, R. Wilcox, T. Rhodes, L. Zeng, Z. Yan, G. McKee, T. Evans, C. Paz-Soldan, P. Gohil, B. Lyons, C. Petty, D. Orlov, and A. Marinoni, "L-H transition trigger physics in ITER-similar plasmas with applied $n = 3$ magnetic perturbations," *Nuclear Fusion* **59**, 126010 (2019).
- ⁵⁷R. P. Seraydarian and K. H. Burrell, "Multichordal charge-exchange recombination spectroscopy on the DIII-D tokamak," *Review of Scientific Instruments* **57**, 2012–2014 (1986).
- ⁵⁸Won-Ha Ko, Seungtae Oh, and Myeun Kwon, "KSTAR Charge Exchange Spectroscopy System," *IEEE Transactions on Plasma Science* **38**, 996–1000 (2010).
- ⁵⁹T. N. Carlstrom, G. L. Campbell, J. C. DeBoo, R. Evanko, J. Evans, C. M. Greenfield, J. Haskovec, C. L. Hsieh, E. McKee, R. T. Snider, R. Stockdale, P. K. Trost, and M. P. Thomas, "Design and operation of the multipulse Thomson scattering diagnostic on DIII-D (invited)," *Review of Scientific Instruments* **63**, 4901–4906 (1992).
- ⁶⁰D. Eldon, B. D. Bray, T. M. Deterly, C. Liu, M. Watkins, R. J. Groebner, A. W. Leonard, T. H. Osborne, P. B. Snyder, R. L. Boivin, and G. R. Tynan, "Initial results of the high resolution edge Thomson scattering upgrade at DIII-D," *Review of Scientific Instruments* **83**, 10E343 (2012).
- ⁶¹K. Lee, J.-W. Juhn, Y. Nam, Y. Kim, H. Wi, S. Kim, and Y.-c. Ghim, "The design of two color interferometer system for the 3-dimensional analysis of

- plasma density evolution on KSTAR,” *Fusion Engineering and Design* **113**, 87–91 (2016).
- ⁶²L. Lao, H. St. John, R. Stambaugh, A. Kellman, and W. Pfeiffer, “Reconstruction of current profile parameters and plasma shapes in tokamaks,” *Nuclear Fusion* **25**, 1611–1622 (1985).
- ⁶³N. C. Logan, B. A. Grierson, S. R. Haskey, S. P. Smith, O. Meneghini, and D. Eldon, “OMFIT Tokamak Profile Data Fitting and Physics Analysis,” *Fusion Science and Technology* **74**, 125–134 (2018).
- ⁶⁴O. Meneghini, S. Smith, L. Lao, O. Izacard, Q. Ren, J. Park, J. Candy, Z. Wang, C. Luna, V. Izzo, B. Grierson, P. Snyder, C. Holland, J. Penna, G. Lu, P. Raum, A. McCubbin, D. Orlov, E. Belli, N. Ferraro, R. Prater, T. Osborne, A. Turnbull, and G. Staebler, “Integrated modeling applications for tokamak experiments with OMFIT,” *Nuclear Fusion* **55**, 083008 (2015).
- ⁶⁵J. C. Hillesheim, W. A. Peebles, T. L. Rhodes, L. Schmitz, T. A. Carter, P.-A. Gourdain, and G. Wang, “A multichannel, frequency-modulated, tunable Doppler backscattering and reflectometry system,” *Review of Scientific Instruments* **80**, 083507 (2009).